Predictive Current Control of Six-Phase IM-Based Nonisolated Integrated On-Board Battery Charger Under Different Winding Configurations

Abdelrahman Habib, Abdullah Shawier, Mahmoud Said Abdel-Majeed, Ayman Samy Abdel-Khalik, *Senior Member, IEEE*, Mostafa S. Hamad, *Senior Member, IEEE*, Ragi A. Hamdy, *Senior Member, IEEE*, and Shehab Ahmed, *Senior Member, IEEE*

***Abstract*—Integrated on-board battery charging (IOBC) constitutes one of the future trends and the potential state-of-the-art technologies proposed for high-power chargers of electric vehicles. Model predictive control has recently been favored in different applications due to its simplicity in defining new control objectives and the straightforward handling of nonlinear constraints. In this article, the predictive current control (PCC) is applied to a six-phase induction-machine-based IOBC with three different winding configurations. From the grid perspective, this article introduces the required winding connections that maximize the charging grid current. Under PCC, different stator phases are controlled to draw balanced three-phase grid currents through controlling the machine nontorque-producing *xy* current components while ensuring zero average/ripple torque production. This article also discusses the effect of winding configuration on the mapping of the 64 available voltage vectors to the $\alpha\beta$, *xy*, and $0^+\ 0^-$ subspaces. The optimal subset voltage vectors of each configuration that achieve the highest possible dc-link utilization, zero torque production, minimum total harmonic distortion (THD), and unity power factor are then introduced. The feasibility to employ the concept of virtual voltage vectors to improve the current quality is also investigated. The three six-phase configurations are obtained from an externally reconfigured 1 kW 12-phase induction motor, which has been used to experimentally validate the theoretical findings.**

***Index Terms*—Asymmetrical six-phase (A6P), dual three-phase (D3P), integrated on-board battery chargers, predictive current control (PCC), six-phase, symmetrical six-phase (S6P), virtual vectors.**

Manuscript received August 8, 2021; revised January 2, 2022; accepted January 31, 2022. Date of publication February 8, 2022; date of current version March 24, 2022. This work was supported by ITIDAs ITAC collaborative funded project under the category type of Advanced Research Projects (ARP) under Grant ARP2020.R29.7. Recommended for publication by Associate Editor T. Shi. *(Corresponding author: Abdullah Shawier.)*

Abdelrahman Habib, Abdullah Shawier, Mahmoud Said Abdel-Majeed, Ayman Samy Abdel-Khalik, and Ragi A. Hamdy are with Electrical Engineering Department, Faculty of Engineering, Alexandria University, Alexandria 21544, Egypt (e-mail: abdelrahman.habib@alexu.edu.eg; eng.abdallh93@gmail.com; es-mahmoud.said1415@alexu.edu.eg; ayman.abdel-khalik@alexu.edu.eg; rhamdy@alexu.edu.eg).

Mostafa S. Hamad is with the College of Engineering and Technology, Arab Academy for Science and Technology and Maritime Transport, Alexandria 1029, Egypt (e-mail: mostafa.hamad@staff.aast.edu).

Shehab Ahmed is with the Computer, Electrical and Mathematical Science and Engineering Division, King Abdullah University of Science and Technology, Thuwal 23955, Saudi Arabia (e-mail: shehab.ahmed@kaust.edu.sa).

Color versions of one or more figures in this article are available at https://doi.org/10.1109/TPEL.2022.3149620.

Digital Object Identifier 10.1109/TPEL.2022.3149620

I. Introduction

ELECTRIC vehicles (EV) industry is expected to share about 30% of the automotive market by 2030 [1]. Battery technology is one of the most important factors that affect the growth of EV in this market. Charging time, weight, cost, and infrastructure constitute the main challenges for EV commercialization. Battery charging concepts can be classified into off-board (fast dc) charging, conventional on-board charging, and integrated on-board battery charging (IOBC) [2]. On-board chargers can directly be connected to the grid, which off-loads the infrastructure requirements. However, their capability of power transfer is significantly limited by several constraints that eventually increase the battery charging time [2]. The IOBC technology exploits the existing propulsion circuit components, particularly the electric motor and inverter, for charging the battery pack instead of adding a bulky separate charging circuit [3] while preserving the on-board charging advantages. IOBC technology provides high-power transfer capability, where the motor is used as an interfacing filter, while the inverter is employed as a bidirectional ac/dc converter [4]. The proper realization of this approach mainly entails zero average torque and pulsating torque production during the charging process, which highly depends on the motor type, the number of phases, the employed controller, and the converter type [5].

Induction motors (IM), switched-reluctance motors (SRM), and permanent magnet (PM) motors have dominated in the EV industry. Thanks to their low cost, reliability, robustness, and low maintenance requirement, several IOBCs proposed in the available literature were based on IM type [6]. On the other hand, permanent magnet synchronous motors (PMSM) have the highest efficiency among all other motor types [7]. As a potential candidate motor type for EV, SRM is praised for its high starting torque and fault tolerance capabilities [8]. During charging, SRMs can produce zero average torque and provide flexible control of energy flow in EV applications [9].

In the available literature, multiphase machines have proved to offer many outstanding merits over three-phase counterparts [10]. The extra degrees of freedom and the decoupling transformations utilized in multiphase machines enable the viable realization of on-board charging of EV, which can effectively ensure zero torque production during charging. Machines with

TABLE I
COMPARISON AMONG POSSIBLE WINDING CONFIGURATIONS OF SPIM

Parameter	D3P	A6P	S6P
Flux Quality [14]	Under $\alpha\beta$ excitation, low order harmonics (5^{th} and 7^{th}) present in the airgap flux. Chorded coils may be used to minimize these harmonic components.	Under $\alpha\beta$ excitation, the lowest order space harmonics are the 11^{th} and 13^{th}. Hence, flux distribution is the best.	Under $\alpha\beta$ excitation, low order harmonics (5^{th} and 7^{th}) present in the airgap flux. Chorded coils may be used to minimize these components.
Current quality [14]	High leakage xy subspace inductance, which improves the current ripple component in the stator current waveform.	The leakage inductance of xy subspace is relatively low; hence, a high ripple current component will likely present.	High leakage xy subspace inductance which improves the stator current waveform.
Postfault Operation [12]	The worst choice in terms of fault tolerance.	A6P is the best choice under isolated neutrals arrangement.	S6P has the higher post-fault capability under connected neutrals arrangement.

multiples of three-phase windings are practically preferred because they can employ readily available three-phase power converters. As a sequence, six-phase machines have gained great attention in many industry sectors. Various configurations of six-phase induction machine (SPIM) have been proposed in the available literature. The asymmetrical six-phase (A6P) configuration has been widely used in high-power drive systems, such as electric ships propulsion system and wind generators [11]. Some recent studies have compared the dual three phases (D3P) and symmetrical six phases (S6P) with A6P configuration under both healthy as well as fault conditions [12], [13]. Abdel-Khalik *et al.* [14] attempt to provide a thorough comparative study among the three variations of six-phase winding configurations by investigating the airgap flux distributions under different excitations. The study showed that the D3P and S6P connections are very similar, whereas the equivalent reactance of an A6P connected winding is slightly higher due to the effect of leakage mutual inductance of a double-layer winding design [14]. In [15], the authors exploit the advantage of S6P under direct controllers, such as predictive current control (PCC), where $\alpha\beta$ voltages can only be generated with zero contributions in other nonfundamental subspaces. An earlier study showed that the PCC of D3P also offers good performance under propulsion mode [16]. Table I lists a brief comparison among the three different SPIM configurations.

The literature has introduced some charging topologies that integrate the six-phase IM with the grid either in isolated or nonisolated configurations. The two topologies of direct grid connection have been introduced in [17] that do not need a separate isolation transformer, where each two phases are tied together forming one phase in the charging mode. In addition, they maximize the charging currents allowing for a charging/propulsion power ratio of 100% at zero average torque. However, a notable ripple torque component is induced due to the pulsating flux component of the $\alpha\beta$ subspace, which causes mechanical vibrations and acoustic noise. On the other hand, several isolated charging configurations for A6P and S6P machines have been introduced in [18] and [19]. In these topologies, a transformer is required to isolate the charging system and provide a multiphase set of voltages.

In the same context, several techniques have been introduced to control multiphase-machine-based IOBC [20]. For slow single-phase charging topologies, the mains are connected between the two neutral points of the three-phase sets and the charging current is regulated by controlling the zero-sequence current component. For three-phase charging, vector space decomposition (VSD) based current control is commonly employed to control the stator current components of different subspaces. Battery charging control is much similar to a grid-tied inverter, where the machine winding acts as an interfacing inductance filter, while the voltage-oriented control is commonly applied under constant voltage or constant current charging modes [17]. In the voltage control mode, the reference *dq* current components are derived based on the dc-link voltage error. While under current control mode, the reference *dq* current components are obtained based on the magnitude of the charging current and power factor. The current control technique based on proportional–integral (PI) controllers has been introduced in [18]. Finally, sophisticated algorithm-based controllers, such as sliding-mode control, model predictive controllers, and fuzzy logic controllers, have shown great advantages over conventional ones [21], including handling nonlinear constraints and ease of considering a multiobjective controller design.

Finite control set model predictive control (FCS-MPC) is the most suitable algorithm to tackle the discrete nature of power electronic converters without the need for a modulation stage [22]. Although these advantages motivated the implementation of PCC in electrical drives and power electronic converters, FSC-MPC suffers from some well-known problems, such as variable switching frequency, tuning of weighting factors, and computational burden [23]. Based on the concept of virtual voltage vectors (VVVs), a novel solution is proposed in the literature, which greatly enhances the optimization stage by creating new voltage vectors (VVs) that eliminate undesirable sequence voltage components [24]. Consequently, the weighting factor design is highly simplified. However, it reduces the dc-link voltage utilization and results in higher switching frequency. Previous research has proposed new techniques to overcome the problem of the variable switching frequency. A duty cycle control technique based on the virtual vector concept is proposed for D3P PMSM [25]. The virtual vectors are synthesized by two basic VVs. Then, the optimal VV is combined with a zero vector to ensure a constant switching frequency. The work done in [26] and [27] presents an FCS-MPC technique for a five-phase drive system in which the optimal virtual vector is selected and its duty cycle is calculated in both $\alpha\beta$ and *xy* subspaces to suppress the current harmonics while ensuring a constant switching frequency. This concept is employed based on the

fact that either isolated D3P or five-phase windings block the flow of the zero-sequence current (0^+ 0^-). Hence, the zero subspace VVs can be optimized to generate a constant switching frequency without disrupting the machine performance.

To the best of the author's knowledge, very limited work has been done to employ predictive control in multiphase-based IOBC application. Sharma *et al.* [21] have taken the initiative to control an S6P-based drivetrain under charging mode using predictive control. Under this latter mode, the stator winding of the six-phase machine is reconfigured as a three-phase winding while power exchange with the grid is carried out using a single three-phase inverter. Hence, line current control is achieved as the conventional three-phase grid-tied inverters. The maximum charging power was, therefore, half that of the propulsion power. This represents, in addition to winding reconfiguration, the main limitations of this winding topology.

This article investigates the PCC control of a six-phase-based nonisolated IOBC employing three different winding configurations, namely, D3P, A6P, and S6P. From practical perspective, A6P has widely been employed in most practical applications. This was mainly dictated from the early days by their better flux distribution when fed from a dual six-step three-phase inverter, a commonly employed technology in old high-power drive systems [28]. With the wide employment of sinusoidal pulsewidth modulated voltage source converters, the justification to employ A6P may now be questionable. As far as the PM machines with fractional-slot concentrated winding tend to be the future trend for EV motor designs, A6P may not be applicable for many interesting slot/pole combinations. Metwly *et al.* [6] have introduced the possible six-phase winding layouts for several slot/pole combinations. Hence, investigating all six-phase winding configurations seems to be mandatory at this stage.

The rest of this article is organized as follows. Section II discusses the required connection for each winding configuration that maximizes the charging line current, ensuring zero average and ripple torque components. In Section III, the VSD is employed to investigate the available VVs and their mapping among the three available $(\alpha\beta)$, (xy), and $(0^+\ 0^-)$ subspaces. The most suitable VVs for charging mode in each configuration have been suggested in Section IV. The experimental validation is carried out in Section V using a double-layer 12-phase induction machine that can be externally reconfigured to form any of the six-phase configurations. Finally, Section VI concludes this article.

II. Proposed Winding Connection

In this section, the required six-phase-based stator winding connections are suggested to achieve balanced high-quality three-phase grid line currents while nullifying the average and pulsating torque components under charging mode.

The changeover between the propulsion and charging modes of operation is simply carried out by exciting the stator winding with a proper sequence current component. A six-phase system constitutes three subspaces, namely, $\alpha\beta$, xy, and $0^+\ 0^-$ subspaces. The VSD transformations that transform the phase quantities to their sequence components with a general arbitrary angle δ are given by (1) and (2).

Under propulsion mode, the controller utilizes the fundamental subspace to drive the SPIM by setting up the fundamental subspace i_α and i_β sequence currents to $I\angle 0^\circ$ and $I\angle -90^\circ$, respectively, while the remaining sequence current components, $i_{xy0^+0^-}$, are set to zero. The corresponding resultant phase currents for all three configurations (D3P, A6P, and S6P), which are obtained from the inverse transformation given by (2), are shown in Fig. 1 (upper phasors). It is clear that the phase angles among the three-phase current sets are 0°, 30°, and 60° for the D3P, A6P, and S3P connections, respectively, under propulsion mode

$$[i_\alpha,\ i_\beta,\ i_x,\ i_y,\ i_{0^+},\ i_{0^-}]^t = T_{\mathrm{VSD}}\ [i_{a1},\ i_{b1},\ i_{c1},\ i_{a2},\ i_{b2},\ i_{c2}]^t \tag{1}$$

On the other hand, the charging mode utilizes the secondary subspace to achieve balanced three-phase grid currents at zero machine torque, assuming a distributed stator winding layout. The control technique in charging mode controls the secondary subspace current components i_x and i_y to be $I\angle 0^\circ$ and $I\angle 90^\circ$, respectively, while the remaining sequence current components $I_{\alpha\beta0^+0^-}$ are set to zero. Fig. 1 (lower phasors) shows the resultant phase currents of the three configurations, where the phase displacements between the two three-phase current sets are 180°, 210°, and 240° for the D3P, A6P, and S6P, respectively, with the same phase sequence as in the propulsion mode.

In order to maximize the grid line currents with minimum winding reconfiguration while ensuring zero developed machine torque, phase current vectors, as shown in Fig. 1 (lower phasors), will be employed to suggest the required stator winding connection under charging. This can be achieved by connecting the end terminals of (a_1 and b_2), (b_1 and c_2), and (c_1 and a_2) together, which maximizes the grid line currents, while ensuring zero $\alpha\beta$ current components. Thus, the line currents will be 1.73, 1.93, and 2 times the phase current magnitude under D3P, A6P, and S6P configurations, respectively, as illustrated in Fig. 1. Hence, the suggested connections of an SPIM-based IOBC connected to the grid (abc_g) with the three configurations (D3P, A6P, and S6P) are shown Fig. 2, where a 12-phase machine has been used to construct the three possible six-phase configurations, as detailed in [14].

III. Voltage Space Decomposition

A nonisolated six-phase-based IOBC connected to the grid can be regarded as a single neutral (1N) six-phase winding assuming a star connected grid. Hence, all upcoming analyses are done based on this conclusion.

For a single neutral inverter fed SPIM, the inverter phase voltages could be obtained based on switching states using (3)

$$\begin{bmatrix} V_{a1} \\ V_{b1} \\ V_{c1} \\ V_{a2} \\ V_{b2} \\ V_{c2} \end{bmatrix} = \frac{1}{6}\ V_{\mathrm{DC}} \begin{bmatrix} 5 & -1 & -1 & -1 & -1 & -1 \\ -1 & 5 & -1 & -1 & -1 & -1 \\ -1 & -1 & 5 & -1 & -1 & -1 \\ -1 & -1 & -1 & 5 & -1 & -1 \\ -1 & -1 & -1 & -1 & 5 & -1 \\ -1 & -1 & -1 & -1 & -1 & 5 \end{bmatrix} S \tag{3}$$

$$S = [\ S_1\ \ S_2\ S_3\ S_4\ S_5\ S_6]^t \tag{4}$$

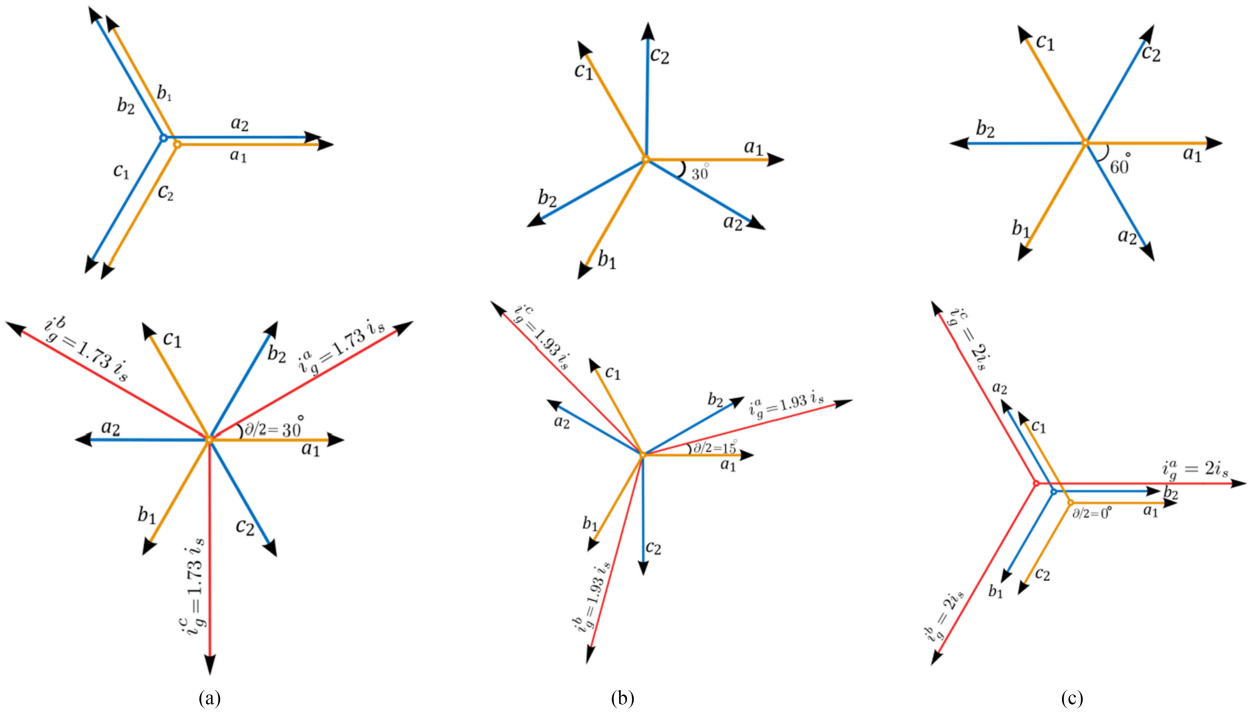

Fig. 1. Phase and line currents of the three configurations of SPIM. (a) D3P, (b) A6P, and (c) S6P, under both propulsion (upper plots) and charging modes (lower plots).

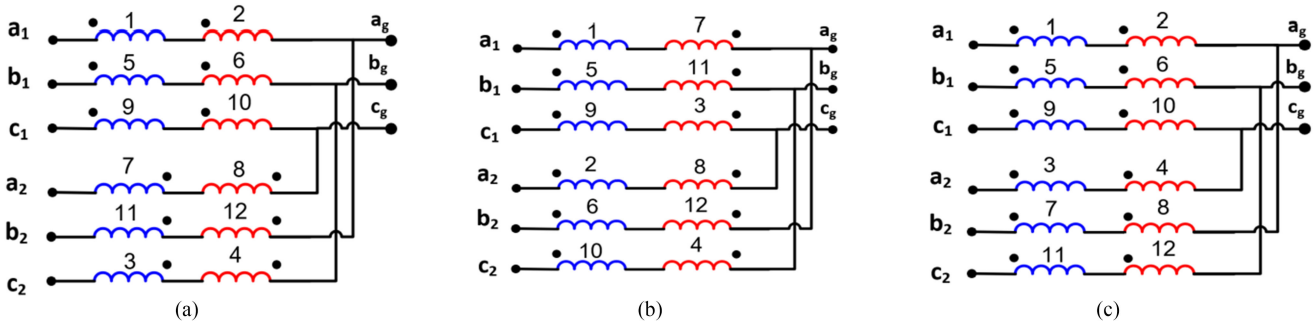

Fig. 2. Proposed connection of a 12-phase stator with grid to integrate the different configurations of an SPIM-based IOBC. (a) D3P. (b) A6P. (c) S6P.

where $S_n \in \{0, 1\}$ is the switching state of leg n. At $S_n = 1$, the upper switch of leg n is ON, while the lower switch will be ON in the case of $S_n = 0$. For a six-phase system, there are 64 switching vectors.

The transformation matrix given by (2) is used to obtain the corresponding sequence voltage components $\alpha\beta\, xy0^+0^-$ of the 64 switching states with an arbitrary angle δ equals 0° , 30°, and 60° for the D3P, A6P, and S6P configurations, respectively. The transformation produces 64 VVs in each subspace, as shown in Fig. 3. The numbering of the VVs is the decimal equivalent of the binary representation of the switching state, while their magnitudes represent the per unit dc-link utilization.

$$T_{\mathrm{VSD}} = \frac{1}{3} \times \begin{bmatrix} 1 & \cos\left(\frac{2\pi}{3}\right) & \cos\left(\frac{4\pi}{3}\right) & \cos\delta & \cos\left(\delta+\frac{2\pi}{3}\right) & \cos\left(\delta+\frac{4\pi}{3}\right) \\ 0 & \sin\left(\frac{2\pi}{3}\right) & \sin\left(\frac{4\pi}{3}\right) & \cos\delta & \sin\left(\delta+\frac{2\pi}{3}\right) & \sin\left(\delta+\frac{4\pi}{3}\right) \\ 1 & \cos\left(\frac{4\pi}{3}\right) & \cos\left(\frac{2\pi}{3}\right) & \cos\delta & -\cos\left(\delta+\frac{2\pi}{3}\right) & -\cos\left(\delta+\frac{4\pi}{3}\right) \\ 0 & \sin\left(\frac{4\pi}{3}\right) & \sin\left(\frac{2\pi}{3}\right) & \cos\delta & -\sin\left(\delta+\frac{2\pi}{3}\right) & \sin\left(\delta+\frac{4\pi}{3}\right) \\ 1 & 1 & 1 & 0 & 0 & 0 \\ 0 & 0 & 0 & 1 & 1 & 1 \end{bmatrix} \tag{2}$$

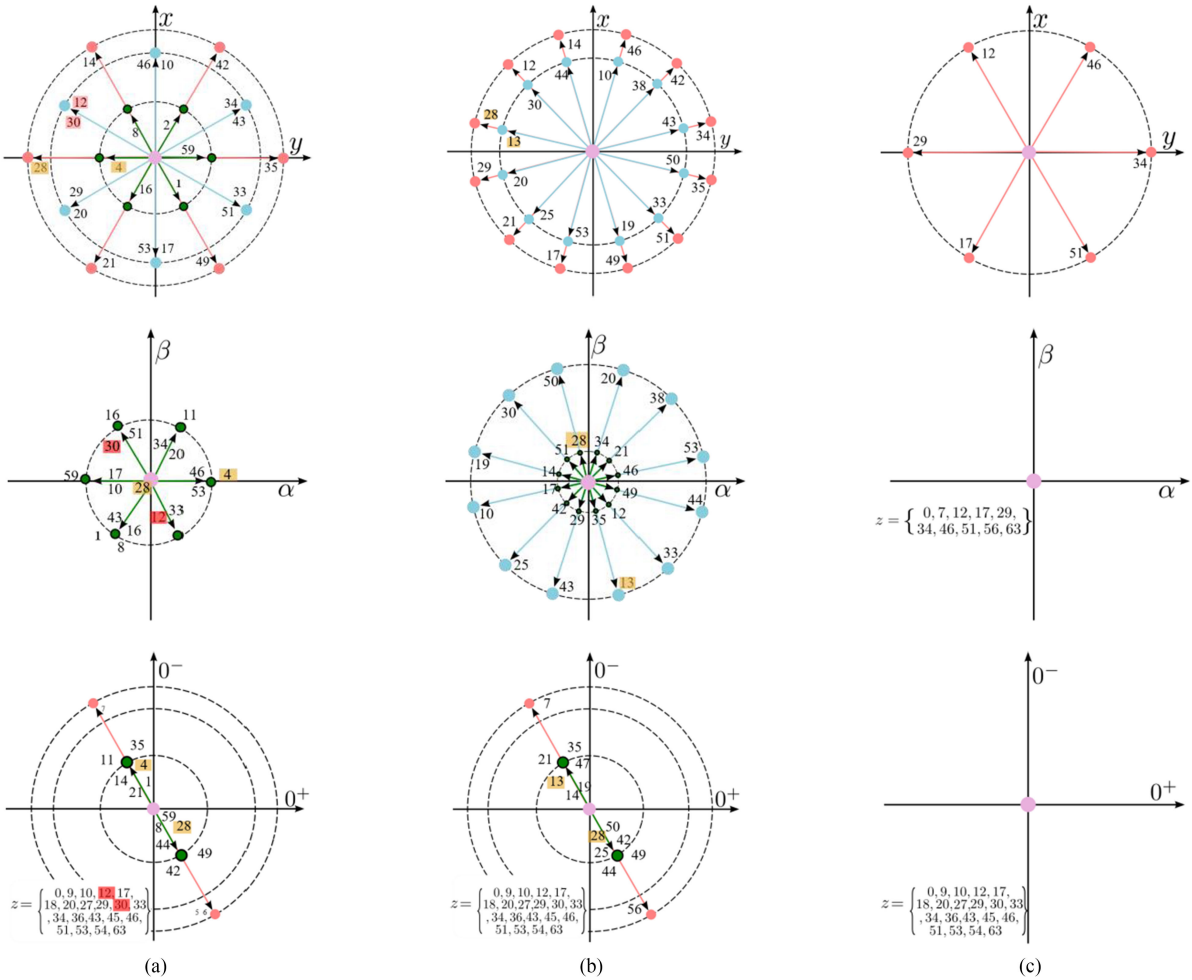

Fig. 3. Feasible VVs for the six-phase-based IOBC. (a) D3P. (b) A6P. (c) S6P.

Considering the secondary subspace xy, which is the dominant subspace under charging, the VVs of the D3P configuration have four different levels, namely, large (L), medium (M), small (S), and zero (Z) with corresponding magnitudes of 0.6667, 0.5774, 0.3333, and 0, respectively. The large level has 6 vectors, the medium level has 12 vectors with only 6 unique directions, the small level has 24 vectors in the same direction of the large vectors, and the zero level has 10 zero-magnitude vectors.

For the A6P, the 64 VVs are mapped into five levels: 12 large vectors, 12 medium-large (ML) vectors, 24 medium (M) vectors, 12 small (S), and 4 zero (Z) vectors and their per unit magnitudes are 0.644, 0.4714, 0.333, 0.1725, and 0, respectively. The voltage levels of the S6P configuration are similar to the D3P but with different numbers of vectors, where the large level has 6 vectors, the medium level has 12 vectors, and the small level has 24 vectors. Tables II and III classify the mapping of the available 64 vectors in each subspace using a color code that indicates the mapping of each vector level in the three subspaces. For instance, the large vectors of a D3P in xy subspace (colored in red) are mapped into zero vectors in $\alpha\beta$ subspace. Another example, the medium vectors of an S6P in xy subspace (colored in blue) are mapped into small vectors in $\alpha\beta$ subspace.

IV. PCC OF IOBC-BASED SPIM

Conceptually, MPC utilizes the system mathematical model to predict the future values of the controlled variables. An objective function is defined as the deviation between the predicted and reference variables for each possible output. Consequently, the MPC algorithm selects the control commands that minimize this objective function [23]. In PCC, the objective function could be represented as the squared error between the reference and the predicted currents for a certain VV. This section investigates the implementation of PCC of an SPIM-based IOBC with the three possible winding configurations. Additionally, it discusses the weighting factor design and the suitable VVs for each configuration.

As mentioned in Section II, the xy current components are controlled based on the required charging current level in the dq reference frame. The block diagram of the proposed controller is shown in Fig. 4. Based on the reference dq current components of the grid, the inverse Park's transformation is used to obtain the reference grid current components $i_g^{\alpha\beta *}$ and the synchronization with the grid is done through a standard phase locked loop. As clear from Fig. 1, the grid line currents are shifted by an angle

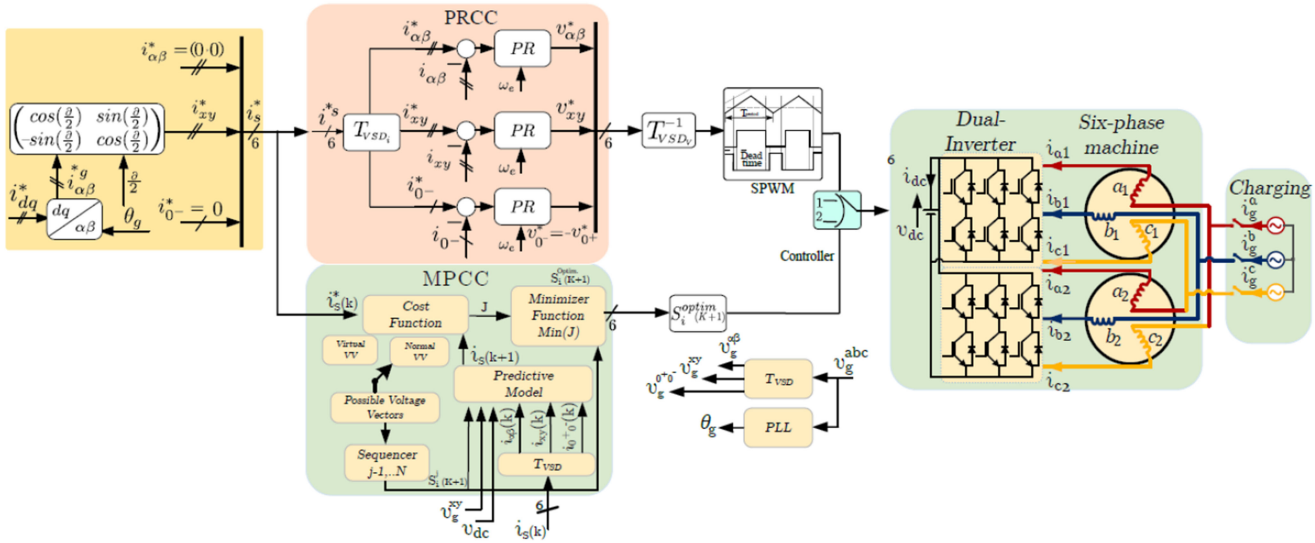

Fig. 4. Block diagram of the SPIM-based IOBC using both conventional PRCC and proposed PCC.

TABLE II
VVs MAPPING TO **xy** AND $\alpha\beta$ SUBSPACES

	Wind. config.	Mag (p.u.)	xy Vectors	$\alpha\beta$ Vectors
D3P	Z	0	[0,7,9,18,27,36,45,54,56,63]	[0,7,14,21,28,35,42,49,56,63]
	S	0.333	[1,2,3,4,5,6,8,11,13,15,16,19, 22,23,24,25,26,31,32,37,38,3 9,40,41,44,47,48,50,52,55, 57,58,59, 60,61,62]	[1,2,3,4,5,6,8,10,12,15,16,17, 20,23,24,29,30,31,32,33,34,3 9,40,43,46,47,48,51,53,55, 57,58,59,60, 61,62]
	M	0.5774	[10,12,17,20,29,30,33,34,43, 46 ,51,53]	[11,13,19,22,25,26,37,38,41, 44 ,50,52]
	L	0.6667	[14,21,28,35,42,49]	[9,18,27,36,45,54]
A6P	Z	0	[0,7,56,63]	[0,7,56,63]
	S	0.1725	[9,11,18,22,26,27,36,37,41,4 5 ,52,54]	[12,14,17,21,28,29,34,35,42, 46 ,49,51]
	M	0.3333	[1,2,3,4,5,6,8,15,16,23,24,31, 32,39,40,47,48,55,57,58,59,6 0,61, 62]	[1,2,3,4,5,6,8,15,16,23,24,31, 32,39,40,47,48,55,57,58,59,6 0,61, 62]
	ML	0.4714	[10,13,19,20,25,30,33,38,43, 44, 50,53]	[10,13,19,20,25,30,33,38,43, 44, 50,53]
	L	0.6447	[12,14,17,21,28,29,34,35, 42,46, 49,51]	[9,11,18,22,26,27,36,37,41,4 5, 52,54]
S6P	Z	0	[0,7,11,22,26,37,41,52,56,63]	[0,7,12,17,29,34,46,51,56,63]
	S	0.333	[1,2,3,4,5,6,8,9,10,15,16,18,2 0,23,24,27,30,31,32,33,36,39, 40,43,45,47,48,53,54,55,57,5 8,59, 60,61,62]	[1,2,3,4,5,6,8,13,14,15,16,19, 21,23,24,25,28,31,32,35,38,3 9,40,42,44,47,48,49,50,55,57, 58,59, 60, 61,62]
	M	0.5774	[13,14,19,21,25,28,35,38,42, 44,49,50]	[9,10,18,20,27,30,33,36,43,4 5, 53,54]
	L	0.6667	[12,17,29,34,46,51]	[11,22,26,37,41,52]

TABLE III
VVs MAPPING TO ZERO SUBSPACE

	Wind. config.	Mag. (p.u)	0^+0^- subspace -Vectors
D3P, A6P, S6P	Z	0	[0,9,10,12,17,18,20,27,29,30,33,34,36,43,45,46,51, 53,54,63]
	S	0.2375	[1,2,4,8,11,13,14,16,19,21,22,25,26,28,31,32,35,37, 38,41,42,44,47,49,50,52,55,59,61,62]
	M	0.4714	[3,5,6,15,23,24,39,40,48,57,58,60]
	L	0.7071	[7,56]

$\partial/2$, where ∂ is the phase angle between a_1 and b_2. To synchronize the reference frame of the machine variables with the grid, the reference $\alpha\beta$ grid current components $i_g^{\alpha\beta *}$ are shifted by the angle $\partial/2$ to obtain the corresponding xy components i_{xy}^* of the machine phase currents. The remaining reference sequence components of the machine currents, $i_{\alpha\beta}^*$, $i_{0^+,0^-}^*$, are set to zero. Finally, all the reference currents are then fed to the PCC algorithm alongside with the current feedback. The conventional proportional–resonant current controller (PRCC) [17] is also shown in Fig. 4, which will be compared with the proposed PCC in the experimental results section.

The PCC algorithm can generally be divided into three major stages: estimation, predictive model, and objective function minimization. The applied PCC algorithm can be summarized as follows.

1) Estimation stage is skipped under charging mode since all desired variables (grid voltages and phase currents) can directly be measured and transformed into sequence currents using (1).
2) The prediction model requires the sequence currents $(i_{\alpha\beta}(k),\ i_{xy}(k),\ i_{0^+0^-}(k))$ along with V_g and $V_{\rm dc}$. The controlled variables are, then, predicted based on the system model for all possible control commands. The next sample $(k+1)$ of the sequence currents is predicted using the corresponding set of VVs as follows:

$$I_{xy}^{K+1} = \left(1 - \frac{R_s T_s}{L_{ls}^{xy}}\right) I_{xy}^{K} + \frac{T_s}{L_{ls}^{xy}} \left(V_{xy} - \mathrm{V}_{\rm grid}^{k}\right) \quad (5)$$

$$I_{\alpha\beta}^{K+1} = \left(1 - \frac{R_s T_s}{L_{ls}^{\alpha\beta}}\right) I_{\alpha\beta}^{K} + \frac{T_s}{L_{ls}^{\alpha\beta}} \left(V_{\alpha\beta}\right) \quad (6)$$

$$I_{0^+0^-}^{K+1} = \left(1 - \frac{R_s T_s}{L_{ls}^{0^+0^-}}\right) I_{0^+0^-}^{K} + \frac{T_s}{L_{ls}^{0^+0^-}} \left(V_{0^+0^-}\right). \quad (7)$$

3) Objective function minimization is concerned with the selection of an optimum VV between the feasible VVs that

minimizes the corresponding objective function in each sample. The weighting factors manipulate the priority of each term in the objective function. The general suggested objective function to ensure balanced xy currents under charging is given as follows:

$$g\ \left(V_s^{k+1}\right) = \left[\left(i_x{}^* - i_x{}^{k+1}\right)^2 + \left(i_y{}^* - i_y{}^{k+1}\right)^2\right] + \gamma\left[\left(i_\alpha{}^* - i_\alpha{}^{k+1}\right)^2 + \left(i_\beta{}^* - i_\beta{}^{k+1}\right)^2\right] + \mu\left[\left(i_{0^+}{}^* - i_{0^+}{}^{k+1}\right)^2 + \left(i_{0^-}{}^* - i_{0^-}{}^{k+1}\right)^2\right] \quad (8)$$

where γ and μ are the weighting factors of the $\alpha\beta$ and 0^+0^- subspaces, respectively, representing their relative priorities in the objective function.

As a matter of fact, the higher the number of constraints in the objective function is, the more difficult the weighting factors design will be. In addition, it becomes more difficult to accurately achieve all the control objectives at the same time. Even though one solution to simplify the objective function design while achieving all the constraints simultaneously is to adopt the concept of elimination of either $\alpha\beta$ or 0^+0^- subspace voltages, or both components, if possible. This is carried out through the proper selection of the appropriate VVs or by applying the virtual voltage concept [24], [29]. In this case, the current constraint of the eliminated subspace voltage can simply be removed from the objective function. This approach highly simplifies the weighting factor design and significantly improves the current quality. Nevertheless, virtual vectors reduce the dc-link utilization and increase the switching frequency. In the following sections, the optimal voltage selection is explained for each winding configuration.

A. Dual Three-Phase Configurations

The VSD of this connection, as introduced in Section III, shows that the largest level of the xy subspace VVs is mapped into zero-magnitude vectors in the $\alpha\beta$ subspace and small vectors in the zero subspace, which highly distorts the motor phase currents due to circulating zero-sequence currents. In order to suppress/eliminate this disrupting zero-sequence voltage component, the concept of virtual vectors can be used to synthesize new VVs having zero magnitude in the 0^+0^- subspace. Consequently, referring to (9)–(14) along with Fig. 3(a), there are two suggested formulas to synthesize these virtual vectors

$$v_{0^+0^-} = f\ (v_n, v_m) = 0 \quad (9)$$

$$v_{0^+0^-} = d_n\ v_{n_{0^+0^-}} - d_m v_{m_{0^+0^-}} \quad (10)$$

$$d_n = 1 - d_m \quad (11)$$

$$d_n = \frac{v_{m_{0^+0^-}}}{v_{n_{0^+0^-}} + v_{m_{0^+0^-}}} \quad (12)$$

where n and m represent the utilized vector level, and d_n and d_m are the duty cycles of vectors v_n and v_m, respectively. The resultant xy and $\alpha\beta$ virtual vector magnitudes could be calculated as follows:

$$v_{\alpha\beta} = \left|d_n v_{n\alpha\beta} - d_m v_{m\alpha\beta}\right| \quad (13)$$

$$v_{xy} = \left|d_n v_{nxy} + d_m v_{mxy}\right|. \quad (14)$$

The first suggested approach is to combine two out-of-phase VVs in the zero subspace, which are simultaneously mapped to two in-phase large and small VVs in the xy subspace, with appropriate ratios to create new VVVs having zero component in the $0^+\ 0^-$ subspace. For example, as shown in Fig. 3(a), the vectors (4, 28) are simultaneously in-phase and out-of-phase in the xy and zero subspaces, respectively. Consequently, combining these two vectors with 0.5 ratios, which are calculated from (9) to (14), will synthesize a VVV with a magnitude of 0.5 p.u. and 0.166 p.u. in the xy and $\alpha\beta$ subspaces, respectively, and with a zero magnitude in the $0^+\ 0^-$ subspace.

The second approach is to combine two redundant in-phase medium VVs in xy subspace with 0.5 ratios making use of the mapping of these VVs into zero-magnitude vectors in the $0^+\ 0^-$ subspace and simultaneously into out-of-phase vectors in the $\alpha\beta$ subspaces. For example, the vectors (12, 30) are in-phase in the xy subspace and are mapped into out-of-phase vectors and zero-magnitude vectors in the $\alpha\beta$ and $0^+\ 0^-$ subspaces, respectively. Accordingly, combining these two vectors synthesizes a new VVV with a magnitude of 0.5774 p.u. in the xy subspace and with a zero magnitude in both $\alpha\beta$ and 0^+0^- subspaces. Consequently, the latter approach is preferred in this article because it produces a higher dc-link utilization and minimizes the harmonics content, which has been experimentally proven.

B. Asymmetrical Configuration

Fig. 3(b) shows that the largest VVs of the xy subspace are mapped into small vectors in the $\alpha\beta$ subspace. Besides, half of these vectors are mapped to the $0^+\ 0^-$ subspace with zero-magnitude vectors, while the other half are mapped as small vectors. Consequently, three approaches can be suggested. The first approach is to utilize the 12 large VVs of the xy subspace and to let the objective function optimizes the three current constraints as minimum as possible through a suitable weighting factor design. The second approach employs the VVV concept to eliminate the $\alpha\beta$ subspace voltage components [24] by combining both the xy large (L) and medium-large (ML) vectors with suitable ratios to synthesize VVVs with zero $\alpha\beta$ components. For example, the vectors (28,13), as shown in Fig. 3(b), are in-phase in the xy subspace and they are mapped into out-of-phase vectors in the $\alpha\beta$ subspace. Hence, with duties cycles of $d_1 = 0.732$ and $d_2 = 0.268$, calculated using (15)–(18), the $\alpha\beta$ components of the corresponding VVV will be zero. Accordingly, the weighting factor γ for the $\alpha\beta$ current components can be removed from the objective function. The resultant VVVs magnitude in xy subspace is reduced to 0.5983 p.u., while their magnitude in 0^+0^- subspace is reduced to 0.1102 p.u.

$$v_{\alpha\beta} = f\ (v_j, v_k) = 0 \quad (15)$$

$$v_{\alpha\beta} = d_j\ v_{j_{\alpha\beta}} - d_k v_{k\alpha\beta} \quad (16)$$

$$d_k = 1 - d_j \quad (17)$$

$$d_j = \frac{v_{k_{\alpha\beta}}}{v_{j_{\alpha\beta}} + v_{k_{\alpha\beta}}} \quad (18)$$

TABLE IV
WEIGHTING FACTOR DESIGN

Weighting factor	D3P	D3P with Virtual VV	A6P	A6P with virtual VV	S6P
γ	0.25	0.1	0.25	0.1	0
μ	0.1	0	0.1	0	0

where j and k represent the utilized vector levels that eliminate the $\alpha\beta$ VVs, and d_j and d_k are the duty cycles of vectors v_j and v_k, respectively.

The third approach is similar to the D3P case in which the selected vectors aim to eliminate the zero-sequence component of the synthesized vectors. In the second approach, large and medium-large vectors are combined under certain ratios to eliminate the $\alpha\beta$ component. However, to eliminate the zero components in the synthesized VVVs, the same vectors are combined under different ratios, which can be calculated from (9) to (14). For example, the vectors (28,13) are in-phase in the xy subspace and they are mapped into two equal and out-of-phase vectors in the 0^+0^- subspace. Consequently, combining these two vectors with 0.5 ratios synthesizes new VVV with a zero magnitude in the 0^+0^- subspace, and the dc-link utilization will be 0.5581, while the $\alpha\beta$ subspace magnitude will be reduced to 0.1494. Hence, two control objectives only exist in the objective function with only one weighting factor γ to determine the priority of $\alpha\beta$ subspace currents relative to the main xy sequence currents. The last approach will be adopted in this article since experimental validation showed that the zero-sequence component highly contributes to the phase current distortion.

C. Symmetrical Configuration

The VSD of symmetrical connection shows that the largest level of the xy subspace VVs is mapped to zero VVs in both $\alpha\beta$ and 0^+ 0^- subspaces, as shown in Fig. 3(c). Therefore, it seems enough to have one term in the objective function to control the xy subspace currents.

Table IV summarizes the weighting factor design for the five different scenarios based on trial and error. The weighting factors of either $\alpha\beta$ or 0^+ 0^- subspaces are set to zero in case their voltage components are eliminated. In some cases, feasible VVs should constitute an $\alpha\beta$ voltage component with suitable magnitude to cancel out any induced $\alpha\beta$ current components, which may exist due to connection asymmetry and/or grid voltage unbalance. Consequently, providing $\alpha\beta$ voltage components may be considered in synthesizing VVV to compensate for these components. However, this point is postponed to a future study.

V. EXPERIMENTAL RESULTS

A. Hardware Setup

In [14], it has been shown that a 24-slot, double-layer 12-phase machine can be used to construct the three possible six-phase configurations by simply reconnecting the stator phases in different manners, as detailed in [14], while preserving the same power rating for the equivalent six-phase stators. The same concept has been used herein to build the required prototype machine,

TABLE V
PROTOTYPE MACHINE SPECIFICATIONS

Parameter	SPIM
Rated RMS phase Voltage (V)	110
Rated Power (Hp)	1.5
Rated RMS phase current (A)	2.8
Rated frequency (Hz)	50
No. of poles	4
Rated speed (RPM)	1400

TABLE VI
PROTOTYPE MACHINE SEQUENCE PARAMETERS

Parameter	A6P	S6P	D3P
R_s	4.18 Ω	4.18 Ω	4.18 Ω
R_r	3.67 Ω	3.46 Ω	3.46 Ω
R_0	14.67 Ω	5.58 Ω	5.52 Ω
$L_{ls}^{\alpha\beta}$	12 mH	9.1 mH	9.1 mH
$L_{lr}^{\alpha\beta}$	16.7 mH	19.1 mH	19.1 mH
$L_{m}^{\alpha\beta}$	247 mH	260 mH	254 mH
L_{ls}^{xy}	7.5 mH	11.8 mH	11.8 mH
L_{ls}^{0}	16.5 mH	26.2 mH	18.2 mH

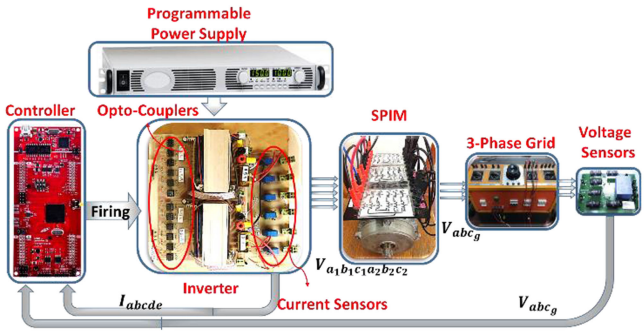

Fig. 5. Experimental six-phase setup.

where the equivalent six-phase machine ratings are listed in Table V . The machine parameters are also estimated based on the analysis given in [14] and are listed in Table VI for the three possible configurations. The mechanical load is simulated using a separately excited dc generator feeding a variable resistive load. The machine is driven using two three-phase intelligent modules with voltage and current ratings of 600 V and 20 A, respectively, and a maximum switching frequency of 20 kHz. A 300 V, 17 A programmable dc supply is used to emulate the required dc link.

Texas instrument launchpad F28379D is used to carry out the proposed PCC of the IOBC system. Feedback measurements are achieved using six current transducers (8 A peak), three voltage sensors, and a hall-effect speed sensor. The experimental setup is shown in Fig. 5. The experimental validation of the three six-phase configurations is given in the following sections. Since a unidirectional programmable supply is used, the power flows from the dc supply to grid (i.e., vehicle-to-grid mode) in all experiments. The reference phase current is set to 4 A (peak) at the unity power factor. Due to hardware limitations, the sampling time T_s is set to 50 μs.

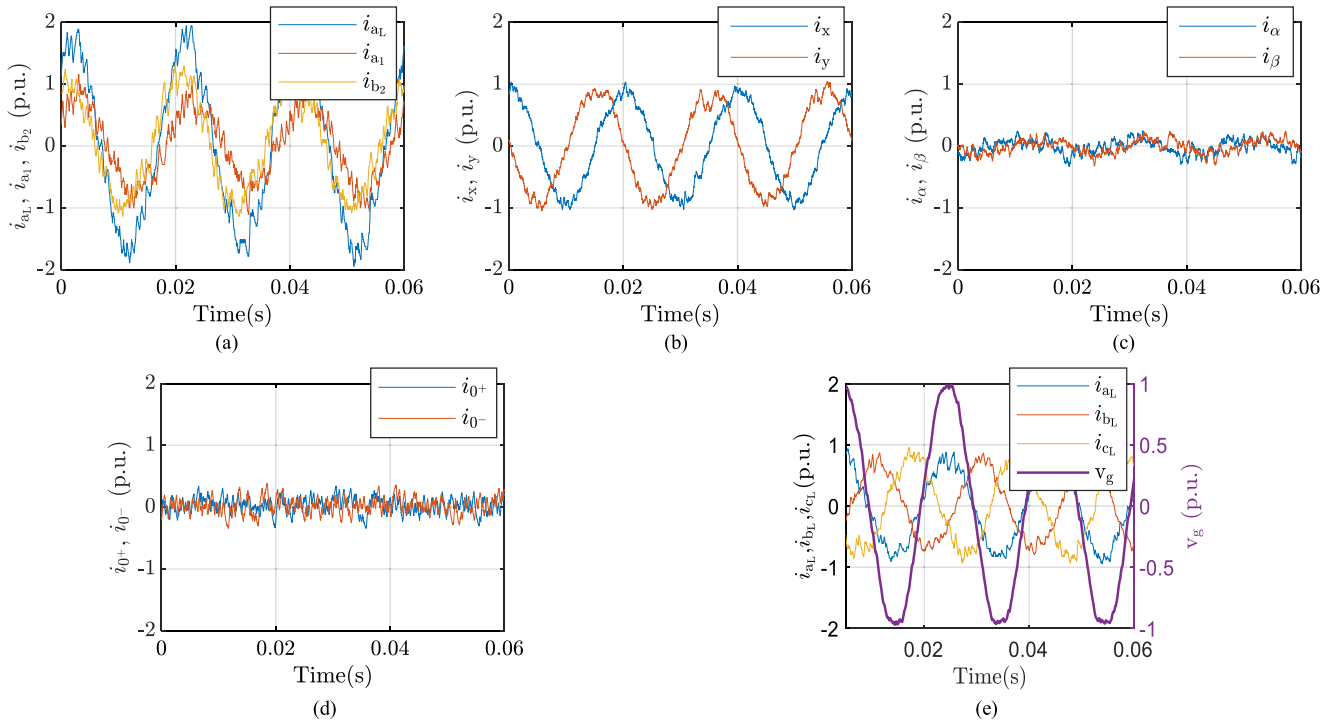

Fig. 6. Performance of D3P-based IOBC under PCC. (a) Phase currents i_{a_1}, i_{b_2} and their resultant grid line current i_{aL}. (b) xy current components. (c) $\alpha\beta$ current components. (d) 0^+0^- current components. (e) Grid line currents and grid phase voltage v_{an}.

TABLE VII
THD OF PHASE AND LINE CURRENTS FOR THE THREE CONFIGURATIONS WITH AND WITHOUT USING VVV CONCEPT AND USING PR CONTROLLER

THD	D3P			A6P			S6P	
Control	Classic PCC	VVV PCC	PR	Classic PCC	VVV PCC	PR	Classic PCC	PR
Phase current	23.42%	9.74%	12.07%	11%	10.65%	6.91%	6.86%	8.64%
Line current	11.04%	7.63%	4.61%	11.28%	10.07%	6.57%	4.8%	6.34%

B. Performance of D3P-Based IOBC

The experimental results of the D3P-based IOBC are shown in Fig. 6. This case offers the lowest line current to phase current magnitude ratio among the three configurations. The line current is 1.73 times the phase currents, while the phase shift angle between phases $\boldsymbol{a}_1$ and $\boldsymbol{b}_2$ is 60°. The maximum charging power is then 86.6% of the machine rated power. Besides, Table VII lists that the phase current is very distorted total harmonic distortion (THD) (THD = 23.42%) compared with the line current, which shows a THD of 11.04%. This is clearly due to the existence of a significant zero-sequence current component. Fig. 6(b) and (c) shows that the machine has almost zero torque-producing $\boldsymbol{\alpha\beta}$ current components, while the $\boldsymbol{xy}$ current components are balanced with a notable distortion. Fig. 7 shows the application of VVV concept, which, in turn, achieves a complete elimination of the zero-sequence current while ensuring zero $\boldsymbol{\alpha\beta}$ current component, as shown in Fig. 7(c) and (d), respectively. Fig. 7(a) shows that the quality of the phase currents is greatly improved (THD = 9.74%), which is, in turn, reflected to a relative improvement in the grid line current, which shows a THD of 7.63%. Table VII summarizes the THD values for all cases. Figs. 6(e) and 7(e) also indicate a unity power factor operation as required.

C. Performance of A6P-Based IOBC

The first option for this case is to apply only the large VVs of the xy subspace, which offers the highest dc-link utilization (0.6447). However, these VVs correspond to nonzero-sequence voltage components in both $\alpha\beta$ and 0^+0^- subspaces. Fig. 8(a) shows the resultant grid line current versus the corresponding phase current when controlling the xy current components to the rated value. As deduced in Section II, the grid line current reaches almost 1.93 of the phase currents while phases a_1 and b_2 are displaced by 30° from each other, which complies with the phasor diagram given by Fig. 1(b). The maximum charging power, in this case, is 96.5% of the machine rated power. The distortion in the phase current as well as the grid line current occurs due to two reasons: the high ripple current component caused by the small value of the secondary subspace inductance L_{ls}^{xy} in the case of an A6P [14], and the low order harmonic content caused by the nonzero-sequence voltage components of the $\alpha\beta$ and 0^+0^- subspaces. This yields a THD in the phase and line currents of approximately 11% and 11.28%, respectively, as listed in Table VII. Fig. 8(b) shows that the xy current components are balanced, while the $\alpha\beta$ and zero-sequence currents are small, as shown in Fig. 8(c) and (d).

Herein, the rationale for using virtual vectors becomes clear as it aims to eliminate the zero-sequence currents in addition to

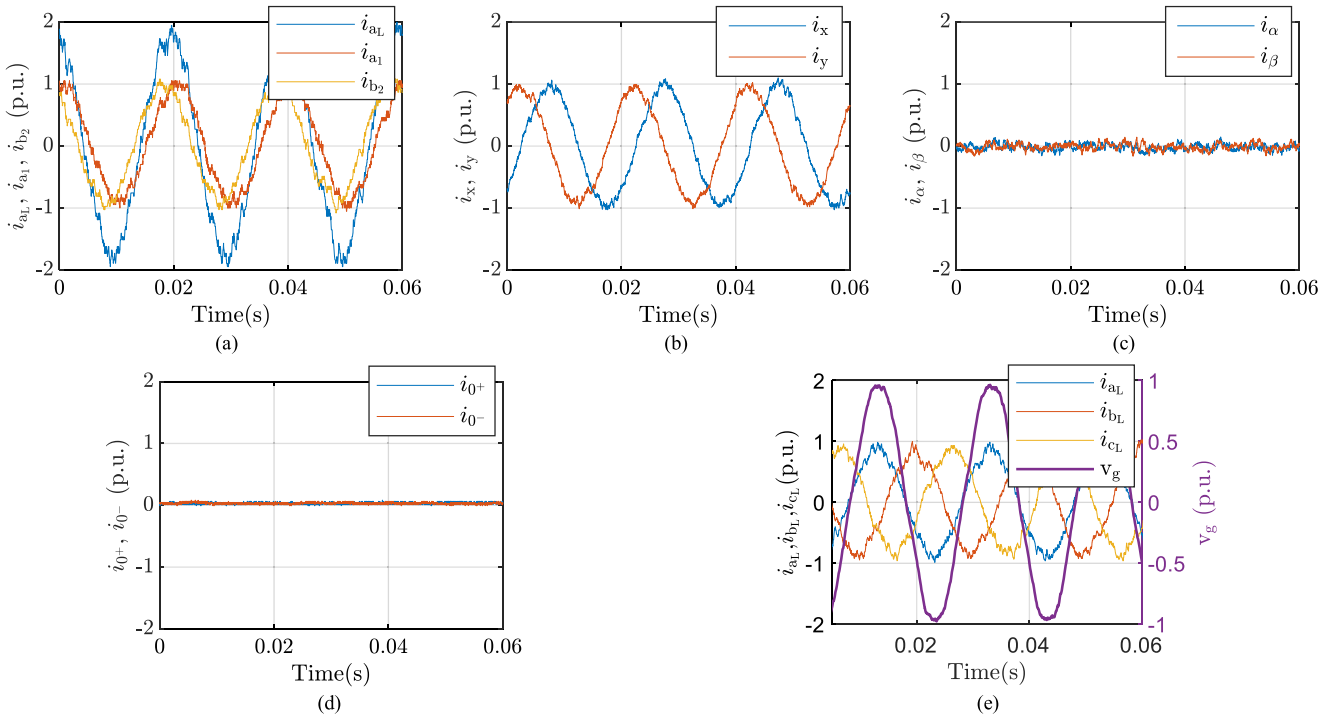

Fig. 7. Performance of D3P-based IOBC under PCC with VVVs. (a) Phase currents i_{a_1}, i_{b_2} and their resultant grid line current i_{aL}. (b) xy current components. (c) $\alpha\beta$ current components. (d) 0^+ 0^- current components. (e) Grid line currents and grid phase voltage v_{an}.

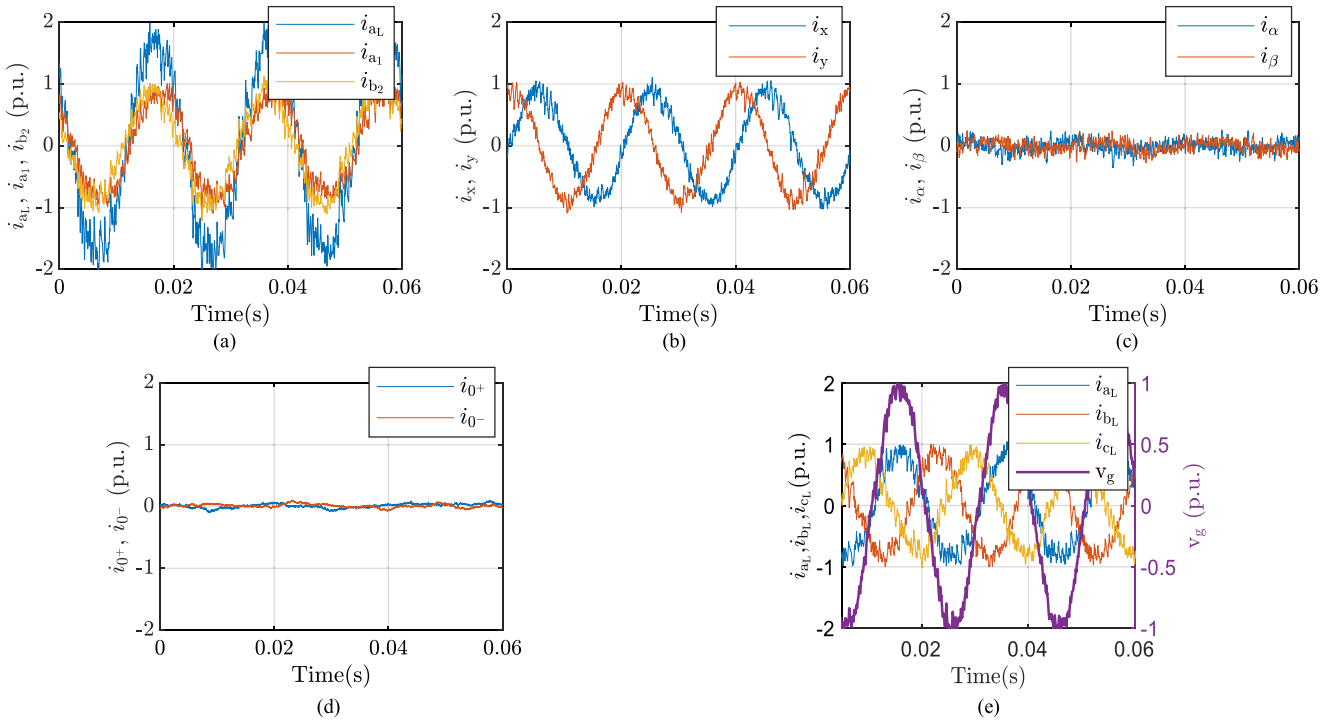

Fig. 8. Performance of A6P-based IOBC under PCC. (a) Phase currents i_{a_1}, i_{b_2} and their resultant grid line current i_{aL}. (b) xy current components. (c) $\alpha\beta$ current components. (d) 0^+ 0^- current components. (e) Grid line currents and grid phase voltage v_{an}.

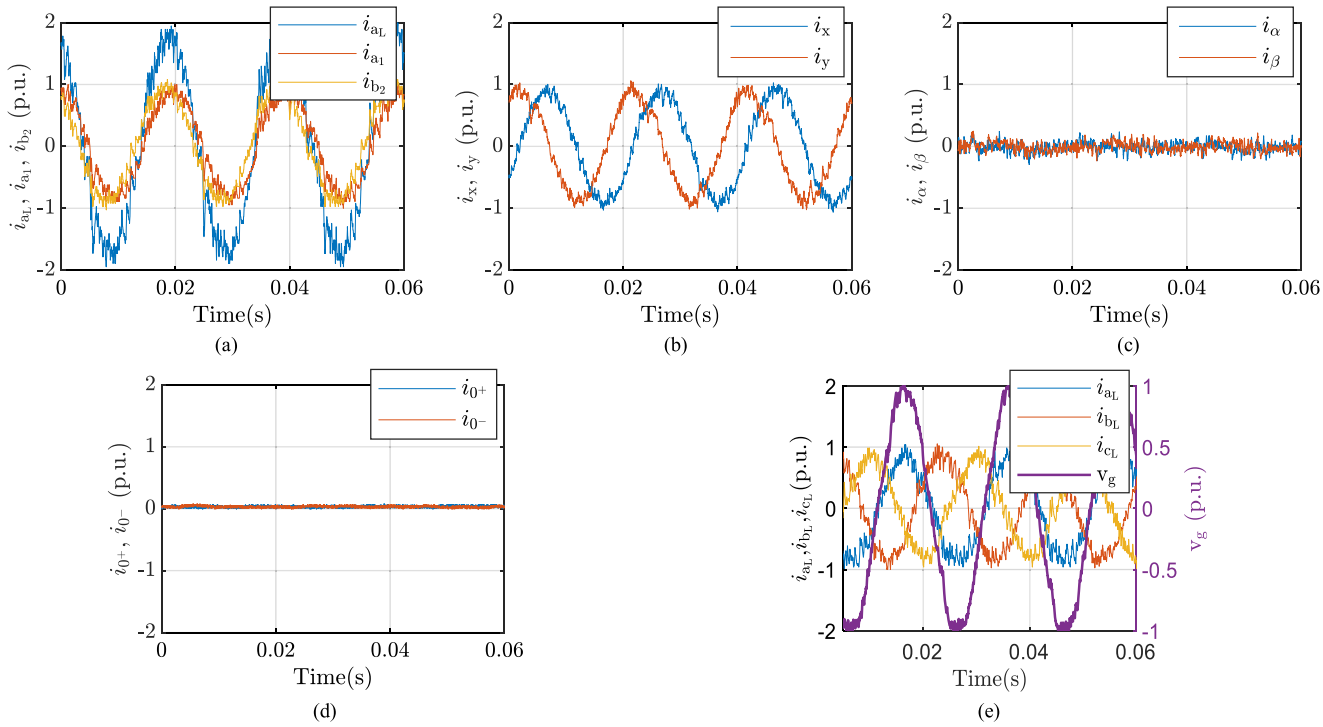

Fig. 9. Performance of A6P-based IOBC under PCC with VVVs. (a) Phase currents i_{a_1}, i_{b_2} and their resultant grid line current i_{aL}. (b) xy component of phase currents. (c) $\alpha\beta$ component of phase currents. (d) 0^+ 0^- component of phase currents. (e) Grid line currents and grid phase voltage v_{an}.

a 20% reduction in the $\alpha\beta$ VVs magnitude. The latter current component can simply be forced to zero by the proper adjustment of the weighting factor. This will relatively improve the quality of the phase and grid line currents, as shown in Fig. 9(a), which, in turn, reduces the THD of the grid line current to approximately 10%. Fig. 9(d) shows that the 0^+0^- subspace component has been eliminated. The dc-link utilization when using the VVV concept is reduced from 0.6447 to 0.558 p.u. Finally, the controller successfully ensures a unity power factor in both cases, as clear from Figs. 8(e) and 9(e). It is fair to say that the obtained improvement seems somewhat marginal due to the high ripple content in the current waveform caused by the small inductance of the *xy* subspace.

D. Performance of S6P-Based IOBC

The experimental results, as shown in Fig. 10, depict that the S6P-based IOBC corresponds to the best current quality, highest grid line current, and the lowest number of VVs. Applying the large VVs only sufficiently results in balanced phase currents as well as line currents. Also, controlling the grid line current through balanced $\boldsymbol{xy}$ current components yield in-phase $\boldsymbol{a_L}$ line current with $\boldsymbol{a_1}$ and $\boldsymbol{b_2}$ phase currents, as shown in Fig. 10(a), while the corresponding line current magnitude becomes double the phase current magnitude at unity power factor, which complies with the phasor diagram, as shown in Fig. 1(c). The battery pack can then be charged at 100% rated machine power.

Needless to say, the current quality in all cases can significantly be improved over the presented cases by simply decreasing the controller sampling time, which was not possible with the current prototype system. Table VIII summarizes the average switching frequency and the computational burden for the five scenarios. Clearly, the S6P-based IOBC offers the lowest switching frequency with the best current waveform.

TABLE VIII
AVERAGE SWITCHING FREQUENCY AND COMPUTATIONAL BURDEN OF EACH TECHNIQUE OF EACH WINDING CONFIGURATION

THD	D3P		A6P		S6P
Control technique	Classic PCC	VVV PCC	Classic PCC	VVV PCC	Classic PCC
Burden time (μs)	30	39	35.3	39	29.3
Avg. switching frequency (kHz)	3.5	4.15	4.2	5.2	3

E. Comparison With PR-Based Current Controller

PR or synchronous-PI-based current controllers are the most employed controllers in most of the available literature. Hence, the proposed PCC is compared with a PR-based current controller to show the main differences. Fig. 11 shows the experimental results of the SPIM-based IOBC for the three connections using the PR-based current controller, as shown in Fig. 4. For a fair comparison with a PCC, the same average switching frequency should be employed. For the proposed PCC, the sampling time employed was 50 μs, which yields an average switching frequency of 3.5 kHz, which has been clarified in Table VIII. This is why the current waveform quality is relatively low. In practical chargers, high switching frequency is commonly employed, which was not available with the employed

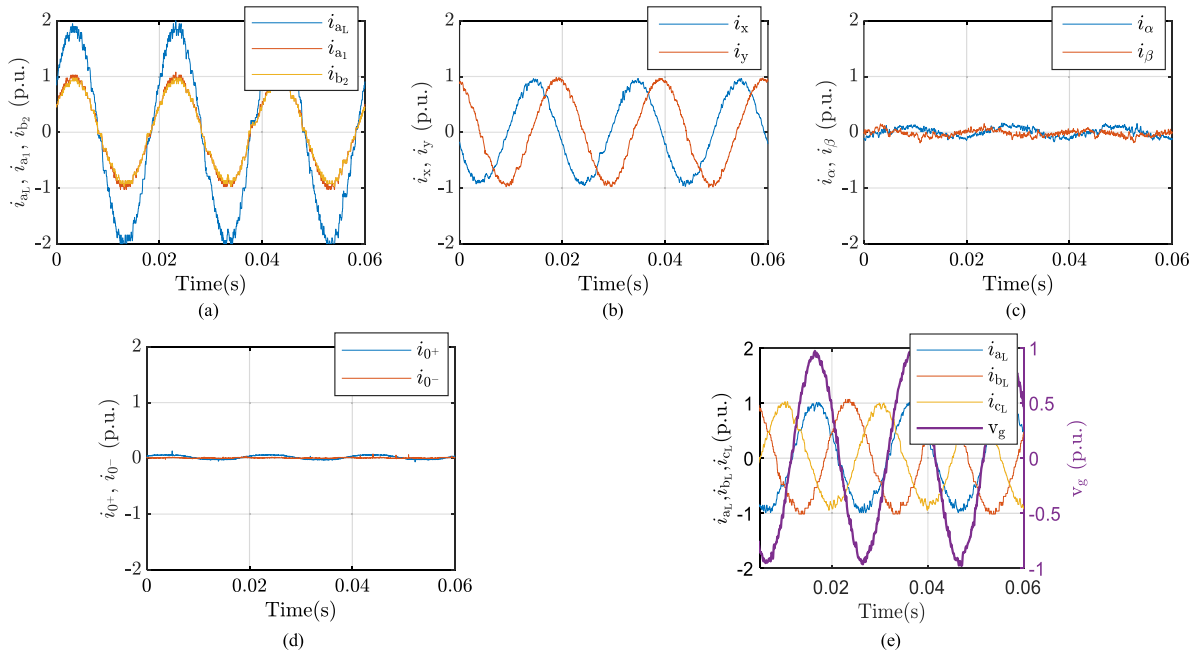

Fig. 10. Performance of S6P-based IOBC under PCC. (a) Phase currents i_{a_1}, i_{b_2} and their resultant grid line current i_{aL}. (b) xy component of phase currents. (c) $\alpha\beta$ component of phase currents. (d) 0^+ 0^- component of phase currents. (e) Grid line currents and grid phase voltage v_{an}.

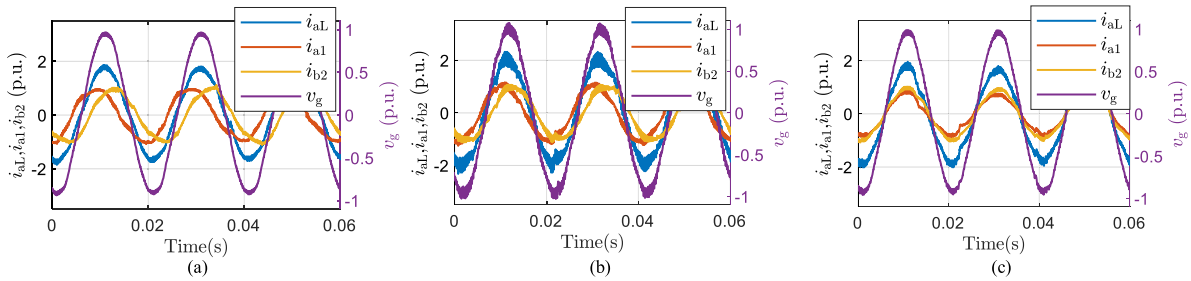

Fig. 11. Performance of SPIM-based IOBC under PR-based current controller. (a) D3P. (b) A6P. (c) S6P (Phase currents i_{a_1}, i_{b_2} and their resultant line current i_{aL}).

prototype system. Based on the THD values, as given in Table VII, the PR-based current controller generally outperforms the PCC for all connections except the S6P case, which offers the best current quality when the proposed PCC is employed. It is also noted that the current waveform under PR-based current control experiences low order harmonics, which can be reduced using harmonic current compensation and with added controller complexity [18].

VI. Conclusion

This article investigated the PCC of a six-phase-based IOBC under different winding configurations. The required stator connections to grid are suggested, which ensure minimum winding reconfigurations, maximum possible line to phase current magnitude ratio, and zero torque-producing current components. The maximum charging power is, therefore, 86.6%, 96.5%, and 100% of the rated machine power for the D3P, A6P, and S6P configurations, respectively. For each winding configuration, the VVs mapping to sequence subspaces as well as the optimal VVs selection were investigated. The concept of virtual VVs has also been employed to improve the current quality while maximizing the dc-link utilization. A comparative case study has been carried out based on experiments to validate the theoretical findings. The results showed that the S6P configuration offers the highest line current magnitude, the best current quality at highest dc-link utilization, the smallest number of VV set, and the lowest average switching frequency. A comparison with a conventional PR-based current controller showed its superiority for all configurations except for the S6P-based IOBC.

References

[1] N. Kittner, I. Tsiropoulos, D. Tarvydas, O. Schmidt, I. Staffell, and D. M. Kammen, "Electric vehicles," in *Technological Learning in the Transition to a Low-Carbon Energy System*. Amsterdam, The Netherlands: Elsevier, 2019, pp. 145–163.

[2] M. Yilmaz and P. T. Krein, "Review of battery charger topologies, charging power levels, and infrastructure for plug-in electric and hybrid vehicles," *IEEE Trans. Power Electron.*, vol. 28, no. 5, pp. 2151–2169, May 2013.

[3] C. Shi, Y. Tang, and A. Khaligh, "A single-phase integrated onboard battery charger using propulsion system for plug-in electric vehicles," *IEEE Trans. Veh. Technol.,* vol. 66, no. 12, pp. 10899–10910, Dec. 2017.
[4] Y. Xiao, C. Liu, and F. Yu, "An effective charging-torque elimination method for six-phase integrated on-board EV chargers," *IEEE Trans. Power Electron.,* vol. 35, no. 3, pp. 2776–2786, Mar. 2020.
[5] I. Subotic, N. Bodo, E. Levi, M. Jones, and V. Levi, "Isolated chargers for EVs incorporating six-phase machines," *IEEE Trans. Ind. Electron.,* vol. 63, no. 1, pp. 653–664, Jan. 2016.
[6] M. Y. Metwly *et al.*, "A review of integrated on-board EV battery chargers: Advanced topologies, recent developments and optimal selection of FSCW slot/pole combination," *IEEE Access*, vol. 8, pp. 85216–85242, 2020.
[7] A. S. Abdel-Khalik, A. Massoud, and S. Ahmed, "Interior permanent magnet motor-based isolated on-board integrated battery charger for electric vehicles," *IET Electr. Power Appl.,* vol. 12, no. 1, pp. 124–134, Jan. 2018.
[8] J. Liang, W. Li, and Z. Song, "Control strategy of integrated charger base on split-winding switched reluctance motor drive," in *Proc. 20th Int. Conf. Elect. Mach. Syst.*, 2017, pp. 1–6.
[9] Y. Hu, C. Gan, Q. Sun, P. Li, J. Wu, and H. Wen, "Modular tri-port high-power converter for SRM based plug-in hybrid electrical trucks," *IEEE Trans. Power Electron.,* vol. 33, no. 4, pp. 3247–3257, Apr. 2018.
[10] A. Shawier, A. S. Abdel-Khalik, R. A. Hamdy, K. H. Ahmed, and S. Ahmed, "Postfault operation of five-phase induction machine with minimum total losses under single open-phase fault," *IEEE Access*, vol. 8, pp. 208696–208706, 2020.
[11] F. Terrien, S. Siala, and P. Noy, "Multiphase induction motor sensorless control for electric ship propulsion," in *Proc. 2nd Int. Conf. Power Electron., Mach. Drives*, 2004, vol. 2, pp. 556–561.
[12] W. N. W. A. Munim, M. J. Duran, H. S. Che, M. Bermudez, I. Gonzalez-Prieto, and N. Abd Rahim, "A unified analysis of the fault tolerance capability in six-phase induction motor drives," *IEEE Trans. Power Electron.*, vol. 32, no. 10, pp. 7824–7836, Oct. 2017.
[13] D. F. V. Garcia, J. Taylor, M. Mohamadian, D. Luedtke, A. Emadi, and B. Bilgin, "A comparative analysis for six-phase motor configurations," SAE Tech. Paper 2020-01-0465, 2020.
[14] A. S. Abdel-Khalik, M. S. Abdel-Majeed, and S. Ahmed, "Effect of winding configuration on six-phase induction machine parameters and performance," *IEEE Access,* vol. 8, pp. 223009–223020, 2020.
[15] A. Gonzalez-Prieto, I. Gonzalez-Prieto, A. G. Yepes, M. J. Duran, and J. Doval-Gandoy, "On the advantages of symmetrical over asymmetrical multiphase ac drives with even phase number using direct controllers," *IEEE Trans. Ind. Electron.*, to be published, doi: 10.1109/TIE.2021.3104588.
[16] A. Shawier, A. Habib, M. Mamdouh, A. S. Abdel-Khalik, and K. H. Ahmed, "Assessment of predictive current control of six-phase induction motor with different winding configurations," *IEEE Access*, vol. 9, pp. 81125–81138, 2021.
[17] I. Subotic, N. Bodo, and E. Levi, "Integration of six-phase EV drivetrains into battery charging process with direct grid connection," *IEEE Trans. Energy Convers.,* vol. 32, no. 3, pp. 1012–1022, Sep. 2017.
[18] I. Subotic and E. Levi, "An integrated battery charger for EVs based on a symmetrical six-phase machine," in *Proc. IEEE 23rd Int. Symp. Ind. Electron.*, 2014, pp. 2074–2079.
[19] I. Subotic, E. Levi, M. Jones, and D. Graovac, "An integrated battery charger for EVs based on an asymmetrical six-phase machine," in *Proc. 39th Annu. Conf. IEEE Ind. Electron. Soc.*, 2013, pp. 7244–7249.
[20] I. Subotic, N. Bodo, E. Levi, B. Dumnic, D. Milicevic, and V. A. Katic, "Overview of fast on-board integrated battery chargers for electric vehicles based on multiphase machines and power electronics," *IET Electr. Power Appl.,* vol. 10, no. 3, pp. 217–229, 2016.
[21] S. Sharma, M. V. Aware, and A. Bhowate, "Symmetrical six-phase induction motor-based integrated driveline of electric vehicle with predictive control," *IEEE Trans. Transp. Electrific.,* vol. 6, no. 2, pp. 635–646, Jun. 2020.
[22] F. Barrero *et al.*, "An enhanced predictive current control method for asymmetrical six-phase motor drives," *IEEE Trans. Ind. Electron.,* vol. 58, no. 8, pp. 3242–3252, Aug. 2011.
[23] S. Vazquez, J. Rodriguez, M. Rivera, L. G. Franquelo, and M. Norambuena, "Model predictive control for power converters and drives: Advances and trends," *IEEE Trans. Ind. Electron.,* vol. 64, no. 2, pp. 935–947, Feb. 2017.
[24] I. Gonzalez-Prieto, M. J. Duran, J. J. Aciego, C. Martin, and F. Barrero, "Model predictive control of six-phase induction motor drives using virtual voltage vectors," *IEEE Trans. Ind. Electron.,* vol. 65, no. 1, pp. 27–37, Jan. 2018.
[25] S. He, Y. Li, Z. Shuai, Y. Zhang, J. Gai, and G. Zhou, "Virtual-vector-based FCS model predictive current control with duty cycle optimization for dual three-phase motors," *J. Phys., Conf. Ser.*, vol. 1754, no. 1, 2021, Art. no. 012083.
[26] C. Xue, W. Song, X. Wu, and X. Feng, "A constant switching frequency finite-control-set predictive current control scheme of a five-phase inverter with duty-ratio optimization," *IEEE Trans. Power Electron.*, vol. 33, no. 4, pp. 3583–3594, Apr. 2018.
[27] C. Xiong, H. Xu, T. Guan, and P. Zhou, "A constant switching frequency multiple-vector-based model predictive current control of five-phase PMSM with nonsinusoidal back EMF," *IEEE Trans. Ind. Electron.,* vol. 67, no. 3, pp. 1695–1707, Mar. 2020.
[28] R. H. Nelson and P. C. Krause, "Induction machine analysis for arbitrary displacement between multiple winding sets," *IEEE Trans. Power App. Syst.,* vol. PAS-93, no. 3, pp. 841–848, May 1974.
[29] J. J. Aciego, I. G. Prieto, and M. J. Duran, "Model predictive control of six-phase induction motor drives using two virtual voltage vectors," *IEEE J. Emerg. Sel. Topics Power Electron.,* vol. 7, no. 1, pp. 321–330, Mar. 2019.

Abdelrahman Habib received the B.Sc. degree in electrical engineering from Alexandria University, Alexandria, Egypt, in 2018.

He is currently a Demonstrator with Electrical Engineering Department, Faculty of Engineering, Alexandria University. His current research interests include electric drives, battery chargers, electric vehicles, embedded systems, and solid-state power conversion.

Abdullah Shawier received the B.Sc. and M.Sc. degrees in electrical engineering from Alexandria University, Alexandria, Egypt, in 2016 and 2021, respectively.

He is currently a Lecturer Assistant with Electrical Engineering Department, Faculty of Engineering, Alexandria University. His current research interests include electric drives, multiphase machine, model predictive control, battery chargers, and power electronics.

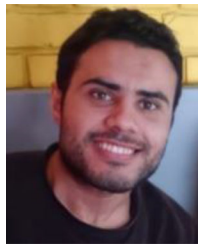

Mahmoud Said Abdel-Majeed received the B.Sc. degree in electrical engineering from Alexandria University, Alexandria, Egypt, in 2019.

He is currently a Researcher with the Faculty of Engineering, Alexandria University. His current research interests include battery chargers, electric vehicles, smart grids, and power electronics.

Ayman Samy Abdel-Khalik (Senior Member, IEEE) received the B.Sc. and M.Sc. degrees from Alexandria University, Alexandria, Egypt, in 2001 and 2004, respectively, and the Ph.D. degree from Alexandria University, Alexandria, Egypt, and Strathclyde University, Glasgow, U.K., in 2009, all in electrical engineering, under a dual-channel program.

He is currently a Professor with Electrical Engineering Department, Faculty of Engineering, Alexandria University. His current research interests include electrical machine design and modeling, electric drives, energy conversion, and renewable energy.

Dr. Abdel-Khalik is the Editor-in-Chief for *Alexandria Engineering Journal* and an Associate Editor for the IEEE TRANSACTIONS ON INDUSTRIAL ELECTRONICS and *IET Electric Power Applications* Journal.

Ragi A. Hamdy (Senior Member, IEEE) received the B.Sc. and M.Sc. degrees from Alexandria University, Alexandria, Egypt, in 1991 and 1994, respectively, and the Ph.D. degree from Heriot-Watt University, Edinburgh, U.K., in 1999.

He is currently a Professor with Electrical Engineering Department, Faculty of Engineering, Alexandria University. His current research interests include electric machines, electric drives, and power electronics.

Mostafa S. Hamad (Senior Member, IEEE) received the B.Sc. and M.Sc. degrees from Alexandria University, Alexandria, Egypt, in 1999 and 2003, respectively, and the Ph.D. degree from Strathclyde University, Glasgow, U.K., in 2009, all in electrical engineering.

From 2010 to 2014, he was an Assistant Professor with the Department of Electrical and Control Engineering, College of Engineering and Technology, Arab Academy for Science, Technology and Maritime Transport, Alexandria, Egypt, where he is currently a Professor. His research interests include power electronics' applications in power quality, electric drives, distributed generation, HVdc transmission systems, and renewable energy.

Shehab Ahmed (Senior Member, IEEE) received the B.Sc. degree from Alexandria University, Alexandria, Egypt, in 1999, and the M.Sc. and Ph.D. degrees from Texas A&M University, College Station, TX, USA, in 2000 and 2007, respectively.

He was with Schlumberger Technology Corporation, Houston, TX, USA, from 2001 to 2007, developing downhole mechatronic systems for oilfield service products. He was with Texas A&M University at Qatar, from 2007 to 2018. He is currently a Professor and a Chair of the Electrical and Computer Engineering Program with Computer, Electrical and Mathematical Science and Engineering Division, King Abdullah University of Science and Technology, Thuwal, Saudi Arabia. His research interests include subsurface mechatronics, solid-state power conversion, electric machines, and drives.